Chemical Physics Letters 857 (2024) 141725

Contents lists available at ScienceDirect

Chemical Physics Letters

journal homepage: www.elsevier.com/locate/cplett

Structure-property relationship of two gamma-lactam derivatives: Hirshfeld surface analysis, DFT, and molecular dynamics simulations

Fan Xue [a], Habbanakuppe D Preetham [b], Rameshwari Verma [a,*], Chandra [c], T.N. Lohith [c], Sahana Raju [d], Divakara S. [e], Mohd Sajid Ali [f], Hamad A. Al-Lohedan [f], Harsha Ramakrishna [g], Kothanahally S. Sharath Kumar [b,*], Vivek Hamse Kameshwar [g,*]

[a] School of Chemistry and Chemical Engineering, Yulin 719000, Shaanxi, China
[b] Department of Studies in Chemistry, Manasagangotri, University of Mysore, Mysuru, India
[c] Department of Physics, The National Institute of Engineering, Manandavadi Road, Mysuru 570008, India
[d] Department of Physics, GSSS Institute of Engineering and Technology for Women, Metagalli, Mysuru, Visvesvaraya Technological University, Belagavi, Karnataka, India
[e] Department of Physics, Vidyavardhaka College of Engineering, Mysuru, Affiliated to Visvesvaraya Technological University, Belagavi, India
[f] Department of Chemistry, College of Science, King Saud University, P.O. Box 2455, Riyadh 11451, Saudi Arabia
[g] Department of Biotechnology, Adichunchanagiri School of Natural Sciences, ACU-CRI, Adichunchanagiri University, B. G Nagara-571448, Karnataka, India

ARTICLE INFO

Keywords:
Gamma-lactam
Hirshfeld surface analysis
DFT
Molecular docking

ABSTRACT

Complete structural and non-covalent interactions of **2a** and **2b** are examined by single crystal X-ray diffraction and computational studies. Hirshfeld surface analysis showed differences in the relative contribution of non-covalent interactions of **2a** and **2b**. Fingerprint plots recognize the major contribution of H···H contacts in **2a** and **2b**. Density functional theory using implicit solvation models, the energy gap of the frontier molecular orbitals found to be 4.624 eV in **2a** and 4.264 eV in **2b**. Docking studies predicted that **2a** and **2b** have suitable structures to target Human Topoisomerase II Alpha, which was further validated using MM/GBSA and MDSs studies.

1. Introduction

The γ-hydroxy-γ-lactams are nitrogen based heterocyclic moieties that are present in a variety of natural compounds and in synthetic drug molecules [1,2]. In 1986, Baldwin *et al.* [3] and researchers from Eli Lilly independently reported the first γ-lactam analogues of penicillins that were effective as antibiotics [4,5]. The γ-lactam ring (also referred as γ-butyrolactam, pyrrolidin-2-one, azolidin-2-one, or 2-oxopyrrolidine) is a core structure in numerous natural and biologically active synthetic compounds. Therefore γ-lactams have been a major focus in medicinal chemistry, consequently various synthetic methods are developed to construct this structural component [6]. Several γ-lactam derivatives exhibit different biological functions, such as acting as an antagonist of the endothelin receptor and preventing the human immunodeficiency virus from activating its integrase activity [7], antioxidant [8] and anti-inflammatory properties [9,10]. Among different γ-lactams, 5-hydroxy-1,5-dihydro-2*H*-pyrrol-2-one (can also referred to as γ-hydroxy-γ-lactam) derivatives have proven to be good bioactive molecules [7,11]. For instance, two natural compounds with 5-hydroxy-1,5-dihydro-2*H*-pyrrol-2-ones in their fundamental structures are myceliothermophins [12], and ianthellidones [9] which are isolated from *Myceliophthora thermophila* and *Ianthella genus* respectively. Furthermore, this structural unit is employed as a building block in synthetic organic chemistry. For example, 5-allyl-5-hydroxy-3-iodo-1*H*-pyrrol-2(5*H*)-one used as a precursor for the total synthesis of the natural compound lucilactaene [13].

Owing to the widespread occurrence of 5-hydroxy-1,5-dihydro-1*H*-pyrrol-2-ones in pharmaceuticals and natural sources [14–16], several synthetic attempts were made to construct 5-hydroxy-1*H*-pyrrol-2(5*H*)-ones. Conventional synthetic methods involve condensation of α,β-diketones and acetamides [17], oxidation of pyrrolidones [18,19], the reaction of chalcones with isonitriles [20], and successive reduction and addition of an organometallic compound to maleimides [21]. In addition, we have recently reported a straightforward approach for the synthesis of 5-hydroxy-1*H*-pyrrol-2(5*H*)-ones from easily accessible starting materials [22]. Our reported method operates in moderate reaction condition that allows sulfur ylide to undergo an intramolecular cyclization with a ketonic carbonyl group followed by a 1,3-hydroxy

* Corresponding authors.
E-mail addresses: rbaghe19@yulinu.edu.cn (R. Verma), sharu.shivaramu@gmail.com (K.S. Sharath Kumar), vivekhamse@acu.ac.in (V. Hamse Kameshwar).

https://doi.org/10.1016/j.cplett.2024.141725
Received 28 July 2024; Received in revised form 20 October 2024; Accepted 22 October 2024
Available online 24 October 2024

Table 1
Crystal data and structure refinement details of the molecules (**2a** and **2b**).

	2a	2b
CCDC	2,157,931	2,157,925
Empirical formula	$C_{17}H_{15}NO_2$	$C_{17}H_{14}BrNO_2$
Formula weight	265.30	344.20
Temperature	294(2) K	294(2) K
Wavelength	0.71073 Å	0.71073 Å
Volume	1385.52(10) $Å^3$	748.4(4) $Å^3$
Space group	P 21/c	P c
Cell dimensions	a = 6.4381(3) Å	a = 13.830(3) Å
	b = 10.5698(4) Å	b = 6.4501(19) Å
	c = 20.3794(8) Å	c = 8.643(4) Å
	β = 92.467(2)°	β = 103.917(11)°
Density(calculated)	1.272 g cm^{-3}	1.527 g cm^{-3}
Z	4	2
Absorption coefficient	0.084 mm^{-1}	2.750 mm^{-1}
F_{000}	560.0	348.0
h, k, l max	8, 14, 27	18, 8, 11
Nref	3441	3533
θ (max)	28.281	28.289
R (reflections)	0.0461 (2318)	0.0683 (1767)
wR2 (reflections)	0.1137 (3441)	0.1875 (3533)

rearrangement, giving good yields of 5-hydroxy-1*H*-pyrrol-2(5*H*)-ones. A variety of lactam derivatives including Camptothecin are known to inhibit topoisomerase [23–26]. Matteo Brindisi *et al.,* reported that the most lipophilic derivatives, bearing the 4-isopropylphenyl or 4-*tert*-butylphenyl group at the γ-lactam nitrogen, proved to be cytotoxic against all the cancer cell lines tested, exerting their greatest activity in SKBR-3 cells, with IC_{50} values of 33 and 18 μM, respectively [27]. DNA topoisomerase enzymes are found across all forms of life and are essential for cellular function [28]. Topoisomerases are vital for maintaining the proper topology of DNA. They achieve this by catalyzing the transient breaking and rejoining of DNA strands, allowing them to pass through each other, relax supercoils, and resolve knots and catenanes [29]. Inhibitors of topoisomerase II are key components of chemotherapy regimens for various types of cancer. For instance, compounds like anthracyclines (e.g., doxorubicin) and epipodophyllotoxins (e.g., etoposide), target Topoisomerase IIα [30]. These inhibitors work by interfering with the enzymatic activity of topoisomerase II, leading to DNA strand breaks and ultimately inducing cell death. They are particularly effective against rapidly dividing cells, which are characteristic of many types of cancer [31].

Computer-aided drug design (CADD) is instrumental in identifying pharmacophoric features and understanding the mechanism of action [32,33]. Molecular docking, MM/GBSA, and molecular dynamics simulations have all proven to be good platforms for the identification of a lead or drug candidate [34]. Therefore, using molecule docking, MM/GBSA, and molecular dynamics simulations together not only offers consistent and complementary signals for predicting structural characteristics but also helps to predict the bioactivity of a drug molecule before it's synthesis and screening [35]. The molecular docking investigations reveal the major interactions of compounds **2a** and **2b** with the Human Topoisomerase II Alpha at the putative binding site of the macromolecule, thereby inhibiting the Human Topoisomerase II Alpha activity.

On the other hand, the structures of **2a** and **2b** were stabilized by different intermolecular interactions including hydrogen bonding N-H···O, and C-H···N interactions. The γ-lactams are significant in the study due to their synthetic relevance; as part of our investigations, compounds **2a** and **2b** were synthesized and characterized their structures by spectroscopic data. Single crystal X-ray diffraction data verify the molecular makeup of **2a** and **2b**. The intermolecular hydrogen bond interactions were analyzed using Hirshfield surface and crystal structure analysis. The molecular charge distribution, chemical reactive characteristics, and molecular structure optimization of **2a** and **2b** were examined using density functional theory (DFT) calculations. In recent decades, DFT has gained attention in drug discovery for its cost-effectiveness and accuracy in predicting the structural, physicochemical, and molecular characteristics of both synthesized and natural compounds. To understand the stability and reactive sites of a molecule, chemical reactivity descriptors, HOMO—LUMO, and electrostatic potential map are determined [36–38].

Herein we explored the conformational characteristics of two gamma lactam derivatives and used *in silico* approach to analyse the binding mode and dynamic properties of ligand and protein. The stability of Human Topoisomerase II Alpha with **2a** and **2b** respectively were evaluated by MDSs to study its stability during simulation. Physicochemical properties, bioavailability, Lipinski's rule and druglikeness of

Table 2
Intermolecular hydrogen bond geometry of molecule (**2a**).

D-H···A	D-H (Å)	H···A (Å)	D···A (Å)	D-H···A (∘)
O2-H20···O1	0.882(19)	1.876(19)	2.7537(16)	173.9(18)
C10-*H*10···O2	0.93	2.30	3.2291(16)	174

Symmetry code: 1-x, −y, 1- z; −1 + x, y, z.

Table 3
Intermolecular and Intramolecular hydrogen bond geometry of molecule (**2b**).

D-H···A	D-H (Å)	H···A (Å)	D···A (Å)	D-H···A (∘)
O1-H20···O2[a]	1.01(18)	1.99(13)	2.714(10)	127(12)
C6-H6···O1[a]	0.93	2.55	3.134(14)	121
C11-H11B···O2[b]	0.97	2.55	2.882(12)	100

Symmetry code: a: x, −1 + y, z; b: x,-y, −1/2z; b-intramolecular interactions.

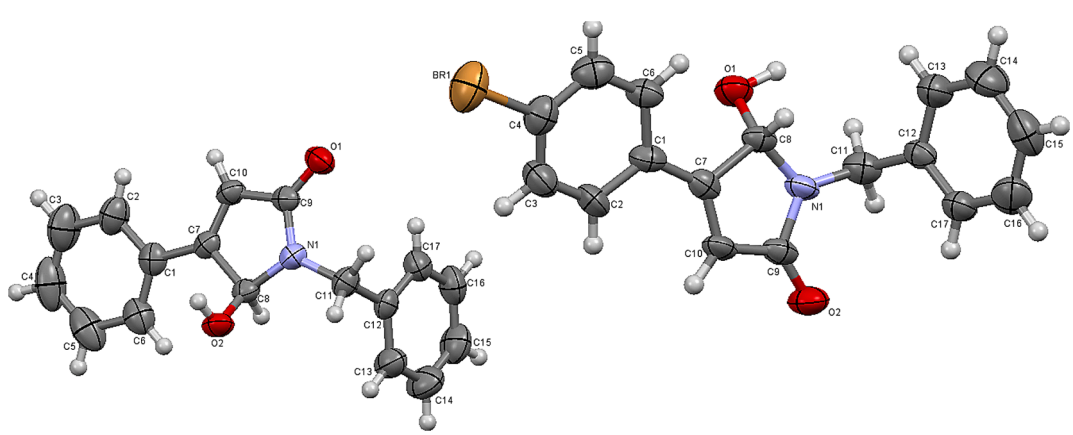

Fig. 1. Structures of **2a** and **2b** with anisotropic displacement ellipsoids drawn at 50% probability level.

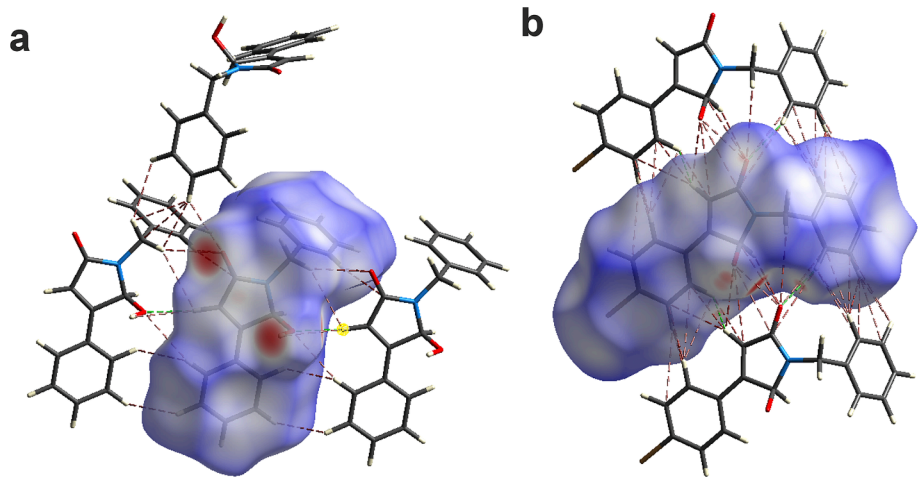

Fig. 2. (a) d_{norm} surface of **2a** and (b) d_{norm} surface of **2b.**

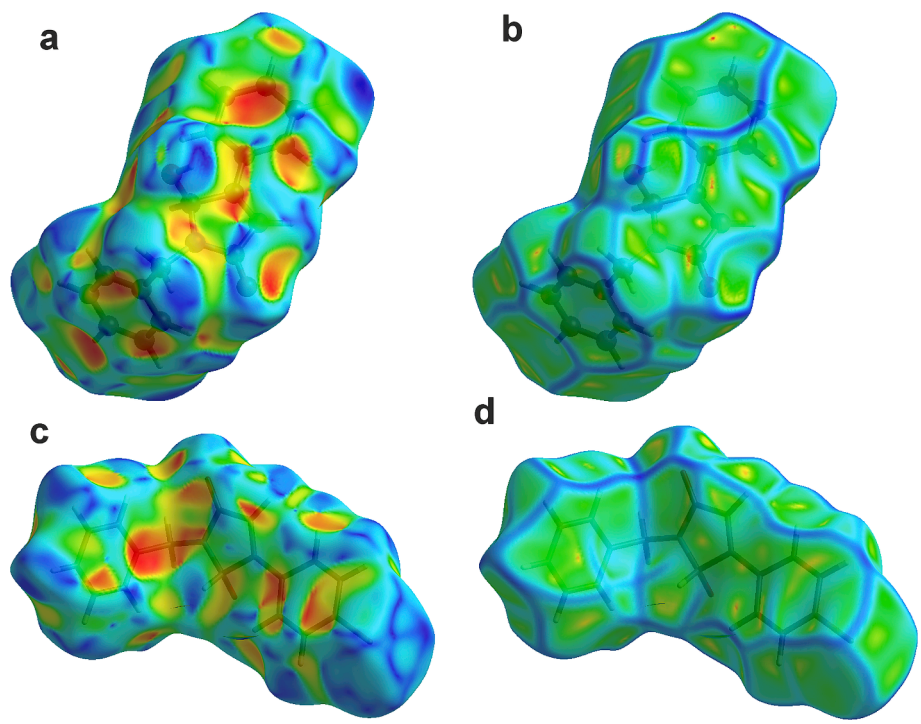

Fig. 3. HS of **2a** mapped over (a) shape index, (b) curvedness. HS of **2b** mapped over (c) shape index (d) curvedness.

compounds **2a** and **2b** were also evaluated by ADME analysis in the current study.

2. Materials and methods

2.1. Synthesis

2.1.1. General procedure for the synthesis of compounds 2a and 2b

1,8-Diazabicyclo[5.4.0]undec-7-ene (DBU, 0.20 mmol) was dropped slowly into a solution of vinyl sulfonyl salt (0.20 mmol) in acetonitrile (5.0 mL) at 0 °C. After 15 min. the reaction was quenched with saturated NH_4Cl solution. The desired compounds were extracted into dichloromethane (3 × 15 mL). The organic layers were dried over anhydrous $MgSO_4$ and evaporated the solvent under reduced pressure. The crude compound was purified by column chromatography on neutral alumina using a dichloromethane/methanol solvent mixture in a 99:1 ratio to yield the desired compound.

Spectral data of compound 2a: White solid; Yield: 93 %; ^{1}H NMR (400 MHz, DMSO-d_6) δ 7.76–7.74 (m, 2H), 7.46–7.42 (m, 3H), 7.36–7.26 (m, 5H), 6.68 (s, 1H), 6.66 (s, 1H), 5.72 (d, J = 9.2 Hz, 1H), 4.80 (d, J = 15.6 Hz, 1H), 4.30 (d, J = 15.6 Hz, 1H). ^{13}C NMR (101 MHz, DMSO-d_6) δ 166.1, 151.4, 133.6, 127.3, 126.1, 125.1, 124.2, 122.8, 119.0, 116.3, 77.1, 37.6. HRMS (ESI-TOF) m/z $[M + H]^+$ calculated for $C_{17}H_{15}NO_2$ 266.1123; found 266.1151.

Spectral data of compound 2b: White solid; Yield: 86 %; ^{1}H NMR (400 MHz, DMSO-d_6) δ 7.67–7.65 (m, 4H), 7.34–7.30 (m, 5H), 6.72 (s, 2H), 5.71 (s, 1H), 4.8 (d, J = 15.6 Hz, 1H), 4.3(d, J = 15.6 Hz, 1H). ^{13}C NMR (101 MHz, DMSO-d_6) δ 169.0, 157.3, 138.6, 131.6, 130.3, 129.1, 128.9, 128.0, 127.5, 120.3, 81.9, 42.3. HRMS (ESI-TOF) m/z $[M (^{79}Br) + H]^+$ calculated for $C_{17}H_{14}^{79}BrNO_2$ 344.0221; found 344.0231; $[M (^{81}Br) + H]^+$ calculated for $C_{17}H_{14}^{81}BrNO_2$ 346.0135; found 346.0188.

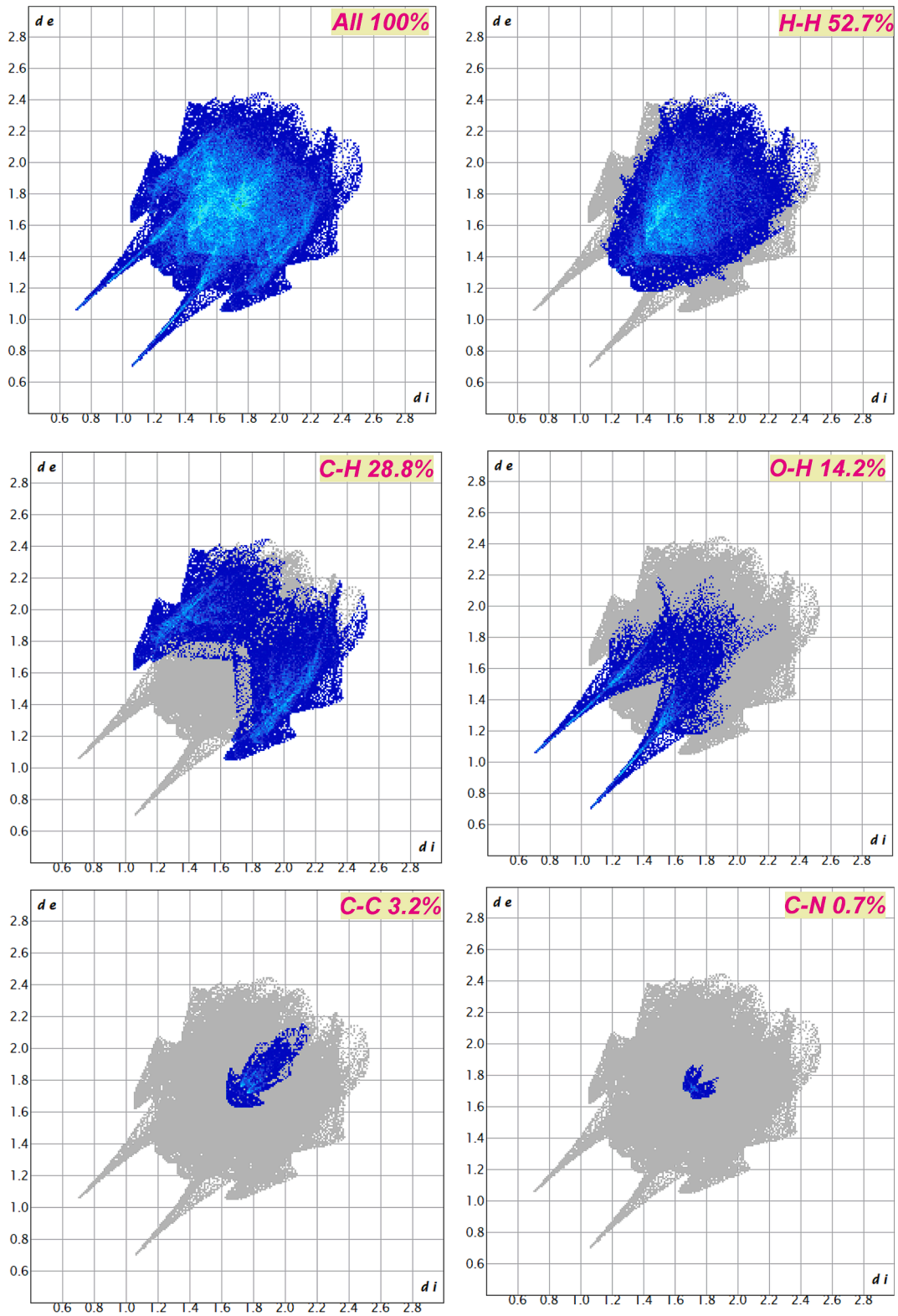

Fig. 4. Selected FP plots of individual intermolecular interaction of **2a** contributed to the total Hirshfeld surface area.

2.2. X-ray diffraction

The X-ray intensity data of compounds **2a** and **2b** were collected on Bruker APEX II CCD diffractometer equipped with the MoKα radiation (λ = 0.71073 Å) at 294(2) K. SADABS software was used for data correction and SAINT software was used for data reduction respectively. The structures were solved by direct methods and refined by full matrix least-squares method against F2 using SHELXS [39] and SHELXL program [40] and the geometrical calculations were carried out using PLATON software [41]. All hydrogen atoms were placed at calculated positions and allowed to ride on their parent atoms. Non-hydrogen atoms were refined anisotropically. The images of ORTEP and packing

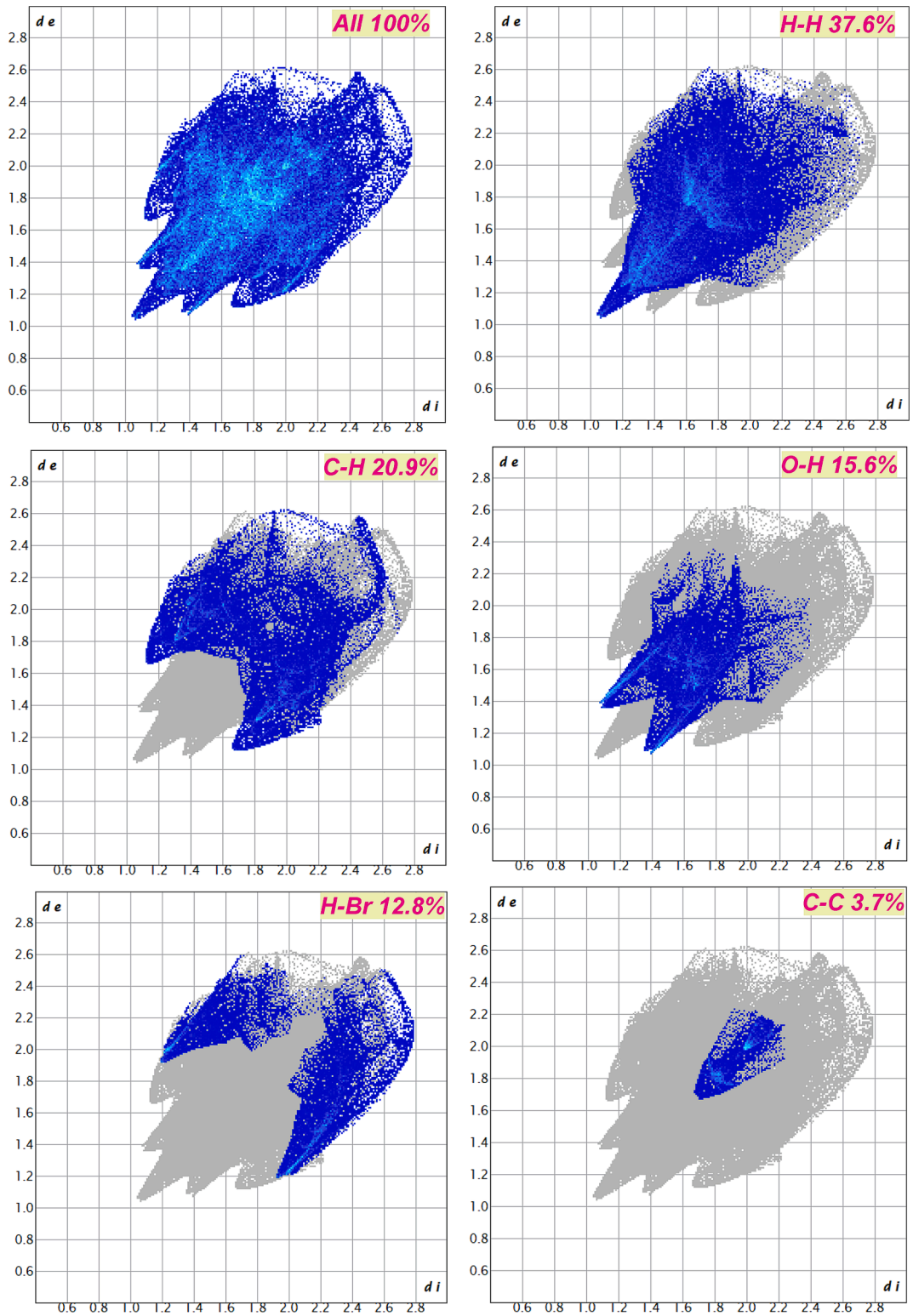

Fig. 5. Selected FP plots of individual intermolecular interaction of **2b** contributed to the total Hirshfeld surface area.

diagrams of molecules **2a** and **2b** were generated using Mercury [42].

2.3. Hirshfeld surface (HS) analysis

The Hirshfeld surface (HS) studies are performed to investigate intermolecular interactions in the crystal structures. The total electron densities of spherical atoms are used to compute the HS, which is reliant majorly on the electron dispersion of a molecule [43]. The HS is specific for a given crystal and electronic environment of spherical atoms. The d_{norm} (normalized contact distance) was found in below given equation. The 2D fingerprint plot summarises the intermolecular contacts present in the crystal [44]. The HS shown in the present findings was produced using Crystal Explorer 21.5 [45].

Table 4
The Summary of individual contacts and their contributions to the total HS.

Type of contacts	Percentage contributions	
	2a	2b
H — H	52.7	37.6
C — H	28.8	20.9
O — H	14.2	15.6
H — Br	–	12.8
C — Br	–	5.4
C — C	3.2	3.7
O — O	–	2.0
C — N	0.7	0.9
C — O	0.3	0.6
N — H	0.2	0.4

$$d_{norm} = \frac{d_i - r_i^{vdw}}{r_i^{vdw}} + \frac{d_e - r_e^{vdw}}{r_e^{vdw}}$$

2.4. Density functional theory (DFT)

DFT calculations for **2a** and **2b** were performed using Gaussian 09 [46] and the results were visualized with Gaussiview 6.0 [47]. The structural coordinates of the compounds **2a** and **2b** are optimized using the DFT/B3LYP/6–311++G(d,p) level of theory in the solvent (Dichloromethane) phase [48], with no symmetry constraints [49].

Frequency calculations were performed on optimized structures to ensure that they were at the minima of potential energy surface (PES). The optimized structure yields the Khon-Sham molecular orbitals, electrostatic potential map, and energies for both compounds.

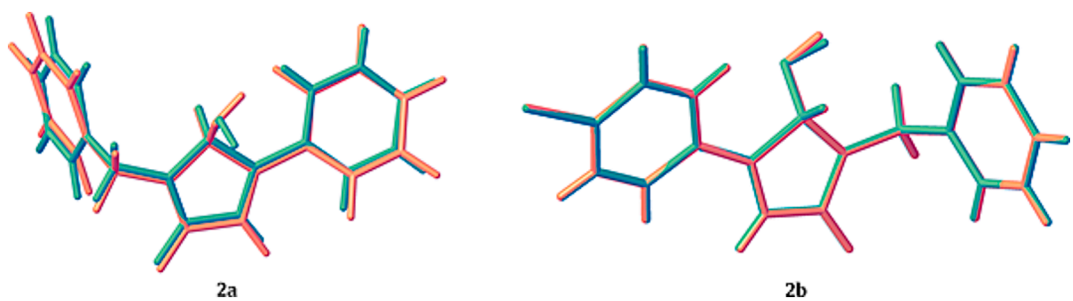

Fig. 6. Superposition of the structures obtained by XRD (pink) and DFT (teal). (For interpretation of the references to color in this figure legend, the reader is referred to the web version of this article.)

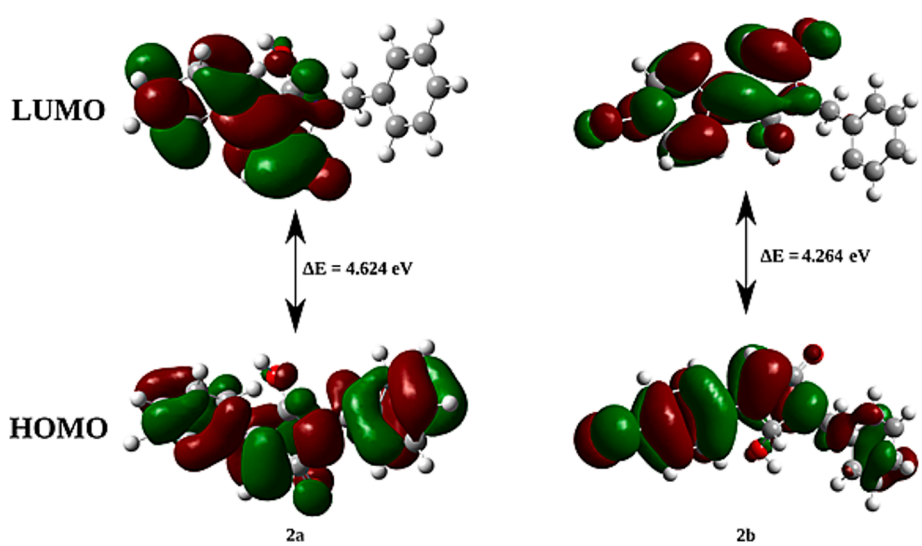

Fig. 7. HOMO-LUMO orbitals of the compounds **2a** and **2b**.

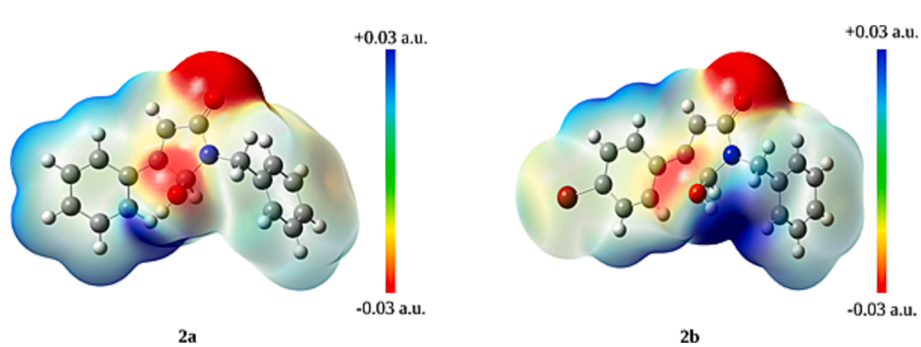

Fig. 8. MEP map of the two molecules **2a** and **2b**.

Table 5
Molecular docking and Molecular mechanics with generalized Born and surface area solvation of ligands **2a** and **2b** with the following targeted proteins.

PDB ID	Ligand	Molecular Docking (kcal/mol)				MM/GBSA ΔG (kcal/mol)				
		Docking Score	Glide (Energy)	Glide (Emodel)	XP Hbond	Total Bind	Coulomb	Hbond	Lipo	vdW
5GWK	2a	−8.33	−44.97	−58.47	−0.70	−37.54	−5.40	−0.53	−17.19	−35.46
	2b	−8.47	−46.35	−62.32	−0.70	−35.42	−7.20	−0.53	−17.19	−32.56
8ELC	2a	−7.33	−44.97	−58.47	0.00	−12.27	−27.89	−0.01	−15.18	−35.28
	2b	−7.48	−36.89	−44.16	−0.70	−8.68	−23.12	−0.06	−13.79	−36.83
7EG1	2a	−7.38	−30.87	−47.16	−0.70	−20.95	−7.14	−0.48	−22.48	−27.84
	2b	−7.25	−39.18	−54.76	−0.70	−28.15	−9.31	−0.54	−19.53	−37.04
1FDW	2a	−6.63	−31.97	−43.41	−0.70	–-	–-	–-	–-	–-
	2b	−7.48	−33.96	−42.08	−0.53	–-	–-	–-	–-	–-
6FNM	2a	−6.79	−35.09	−47.07	−0.84	–-	–-	–-	–-	–-
	2b	−6.32	−35.97	−45.26	−0.00	–-	–-	–-	–-	–-
3VP0	2a	−2.90	−34.87	−45.28	−0.33	–-	–-	–-	–-	–-
	2b	−3.15	−31.55	−40.77	−0.26	–-	–-	–-	–-	–-
8HID	2a	−4.13	−27.10	−31.65	−1.04	–-	–-	–-	–-	–-
	2b	−4.02	−32.10	−34.04	−0.12	–-	–-	–-	–-	–-
1UKI	2a	−5.82	−33.75	−45.68	0.00	–-	–-	–-	–-	–-
	2b	−5.86	−34.40	−47.63	−0.47	–-	–-	–-	–-	–-
7K2F	2a	−4.03	−33.55	−44.52	−0.61	–-	–-	–-	–-	–-
	2b	−4.08	−32.89	−43.21	−0.70	–-	–-	–-	–-	–-
8OK0	2a	−5.14	−29.89	−38.96	−0.70	–-	–-	–-	–-	–-
	2b	−4.43	−30.95	−40.29	−0.70	–-	–-	–-	–-	–-
6HKQ	2a	−3.18	−28.61	−33.73	−0.35	–-	–-	–-	–-	–-
	2b	−3.58	−30.35	−36.23	−0.35	–-	–-	–-	–-	–-
5CVO	2a	−1.16	−29.58	−36.48	−0.35	–-	–-	–-	–-	–-
	2b	−0.70	−31.71	−38.67	−0.35	–-	–-	–-	–-	–-
4ZKA	2b	−3.93	−29.20	−30.08	−0.72	–-	–-	–-	–-	–-

Koopman's approximation [50] is used to estimate the HOMO-LUMO energy gap and associated reactive characteristics such as electronegativity, chemical potential, hardness, softness, and electrophilicity. A molecular electrostatic potential (MEP) map was utilized to view and understand the molecule's charge distribution and reactive sites present in molecules **2a** and **2b** [51].

2.5. Molecular docking and molecular dynamic simulations

The molecular docking procedure was carried out as per the literature method [52]. A series of crystal structures of protein, namely Human topoisomerase II alpha, PDE3A, JNK2, Ephrin B4 (EphB4) Receptor Protein Kinase, Human 17β-Hydroxysteroid-Dehydrogenase, glutaminase, catalase, JNK1, human KEAP1, human NQO1, GPX4, and ubiquitin with their pdb id are 5GWK, 7EG1, 8ELC, 6FNM, 1FDW, 3VP0, 8HID, 1UKI, 7K2F, 8OK0, 6HKQ, 5CVO, and 4ZKA respectively were imported into workspace. The coordinates were acquired from the protein data bank. Each protein was generated using a standard set of parameters, which involved automated bond creation, bond orders, hybridization, explicit hydrogen, and charge assignments. Additionally, water molecules near heteroatoms exceeding 5 Å were eliminated from the proteins. We utilized the protein preparation wizard to get each protein ready, keeping the catalytic water molecules at the active site, and then applied an OPLS3 force field for restrain minimization based on reference [53]. To ensure convergence of the large atoms during the protein pre-processing for docking in the maestro's prime module, we set the root-mean-square deviation (RMSD) at 0.30 Å. Once the protein was prepared, we computed a grid generation with a 20 Å separation from the active site. DFT optimized structure of **2a** and **2b** was used to dock into a receptor grid with a radius of 20 Å using extra-precision docking, and docking calculation was then evaluated using the docking score [54–56].

2.6. MM/GBSA calculation

The strength of the connection and the influence of specific changes on how a ligand binds are evident in the binding energy (ΔG_{Bind}) of a protein and a ligand. The top scorer in molecular docking protein–ligand adduct was used to evaluate for MM/GBSA. The Prime MM/GBSA module in Mäestro was used in this investigation to predict ΔG_{Bind} [57]. The posture viewer data for the docked complex has been posted to the MM/GBSA panel. We used the OPLS3 force field and applied the VSGB 2.0 solvation model [58]. $\Delta G_{(bind)}$ was calculated as below

$$\Delta G_{(bind)} = E_{complex}(\text{minimized}) - \left[E_{ligand}(\text{minimized}) + E_{receptor}(\text{minimized})\right]$$

where ΔG_{Bind} is binding free energy and $E_{complex}$(minimized), E_{ligand}(minimized), and $E_{receptor}$(minimized) are minimized energies of receptor-ligand complex, ligand, and receptor, respectively [59].

2.7. Molecular dynamic simulations (MDSs) and ADME

This study conducted MDSs on a 64-bit Ubuntu 20.04 platform in the Maëstro 9.1 software [57,60]. The molecular docking and MM/GBSA promising scores for **2a** and **2b** ligands were taken for MDSs. The docked human topoisomerase II alpha complexed with ligand was chosen for MDSs. The complex was socked using the TIP4P water model using the system-builder option in the solvated orthorhombic periodic boundary of the box. To neutralize the complex, Mg^+ ions (1.719 mM, with a charge of + 4) were added, Na^+ ions (60.175 mM, with a charge of + 140), and Cl^- ions (50.719 mM, with a charge of −118) were added. The Desmond program's default relaxation technique performed MDSs and a periodic boundary condition in the number of atoms, pressure, and temperature (NPT) ensemble, 310 K as the temperature and 1 atmosphere as the pressure. The RMSD and total energy of the complexes were examined using simulation-interaction plots. The simulation was done for up to 200 ns [61]. ADMET was calculated using the Swissadme web tool for the synthesized molecules [62].

3. Results and discussion

3.1. X-ray crystallography and spectroscopic data

The crystal structures of **2a** and **2b** molecules show that they crystallize in a monoclinic system with the space groups P 21/c for **2a** and P

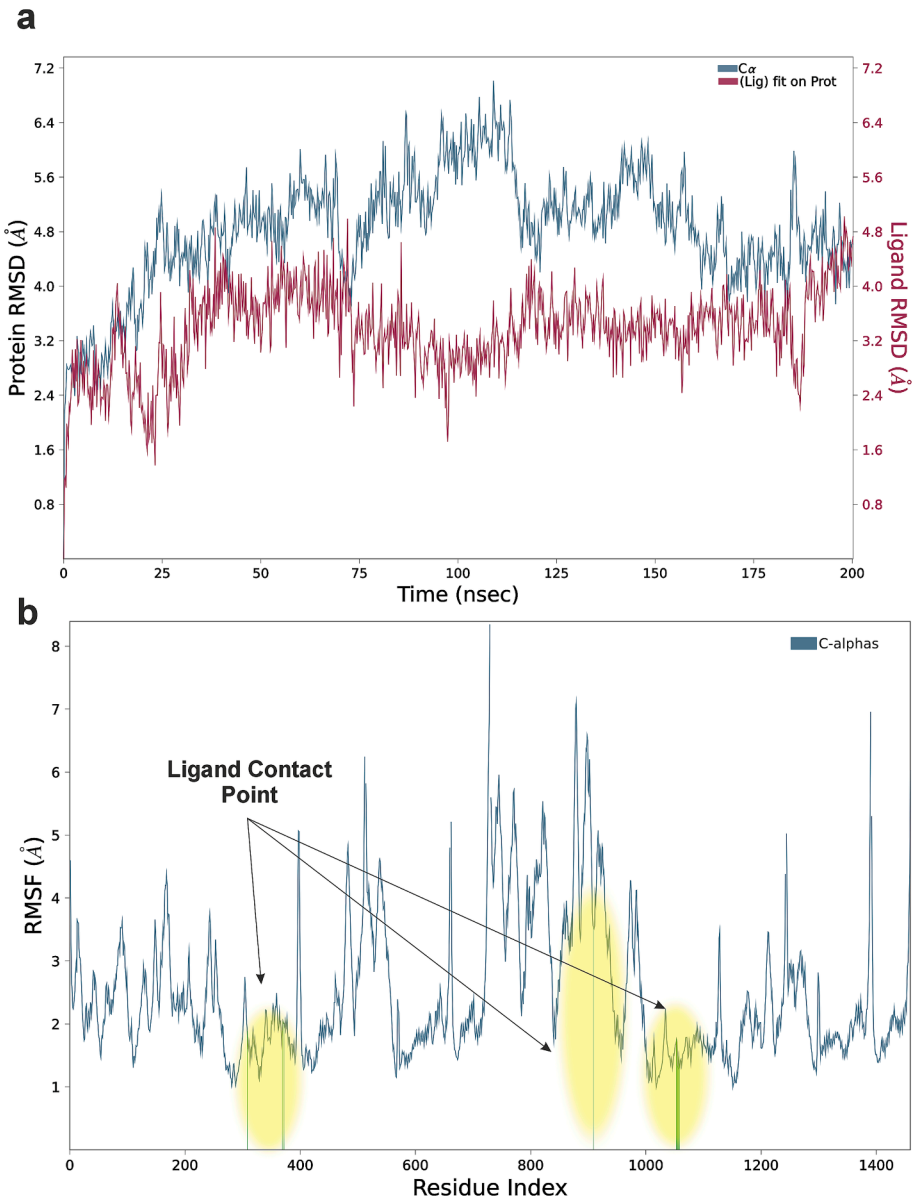

Fig. 9. (**a**) Topoisomerase IIα and compound **2a** RMSD plot. (**b**) Protein RMSF plot to show ligand contact point (green) with amino acid residues of Human Topoisomerase IIα. (For interpretation of the references to color in this figure legend, the reader is referred to the web version of this article.)

c for **2b** respectively. The complete crystal data and structure refinement of molecules **2a** and **2b** are tabulated in Table 1. The ORTEP representation of the compounds (**2a** and **2b**) drawn at 50 % probability is shown in Fig. 1 and the packing representation of both the molecules is shown in Fig. S1**a-b**. They differ only in their substituent at the 4th position of the pyrrole-2-one ring. The crystal structure of **2a** is stabilized by O-H···O, C-H···O intermolecular interactions and **2b** is stabilized by O-H···O, C-H···O intermolecular interactions and C-H···O intramolecular interactions. The summary of the geometry details of hydrogen bond interactions of the compounds **2a** and **2b** are given in Tables 2 and 3 respectively.

In addition, the number of protons, coupling constants, and splitting patterns in the ^{1}H NMR spectra of **2a** and **2b** are precisely matched with the corresponding structures of **2a** and **2b**. ^{1}H NMR spectrum of **2a** contains 10 protons in the aromatic region (δ 7.76 ppm to δ 7.26 ppm as multiplets) corresponds to two mono-substituted benzene rings in the structure. OH proton resonates at δ 6.68 ppm as a singlet, proton on C-3 carbon atom in pyrrole-2-one ring appeared at δ 6.66 ppm as a singlet whereas proton on C-5 carbon resonate at δ 5.72 ppm as a doublet. The remaining two benzylic protons appeared as doublet with same coupling constants at δ 4.80 ppm and δ 4.30 ppm respectively. ^{1}H NMR spectrum of **2b** contains 9 protons in the aromatic region (δ 7.67 ppm to δ 7.30 ppm as multiplets) corresponds to one mono-substituted and another di-substituted benzene rings in the structure. OH proton and proton on C-3 carbon atom in pyrrole-2-one ring appeared at δ 6.72 ppm as singlets, whereas proton on C-5 carbon resonate at δ 5.71 ppm as singlet. The remaining two benzylic protons appeared as doublet with same coupling constants at δ 4.80 ppm and δ 4.30 ppm respectively. The number of carbon signals in ^{13}CNMR spectra also matches well with the **2a** and **2b** structures. A base peak at m/z 266.1151 (M^{+}+1) in the high-resolution mass spectrum (HRMS) of **2a** is consistent with the molecular structure of this compound. The molecular ion cluster peaks at m/z 344.0231 (M^{+}) and 346.0188 (M^{+}+2) in almost 1:1 ratio in the HRMS spectrum of **2b** correlates with the molecular weight of compound **2b** and also suggests the presence of one bromine atom in its structure.

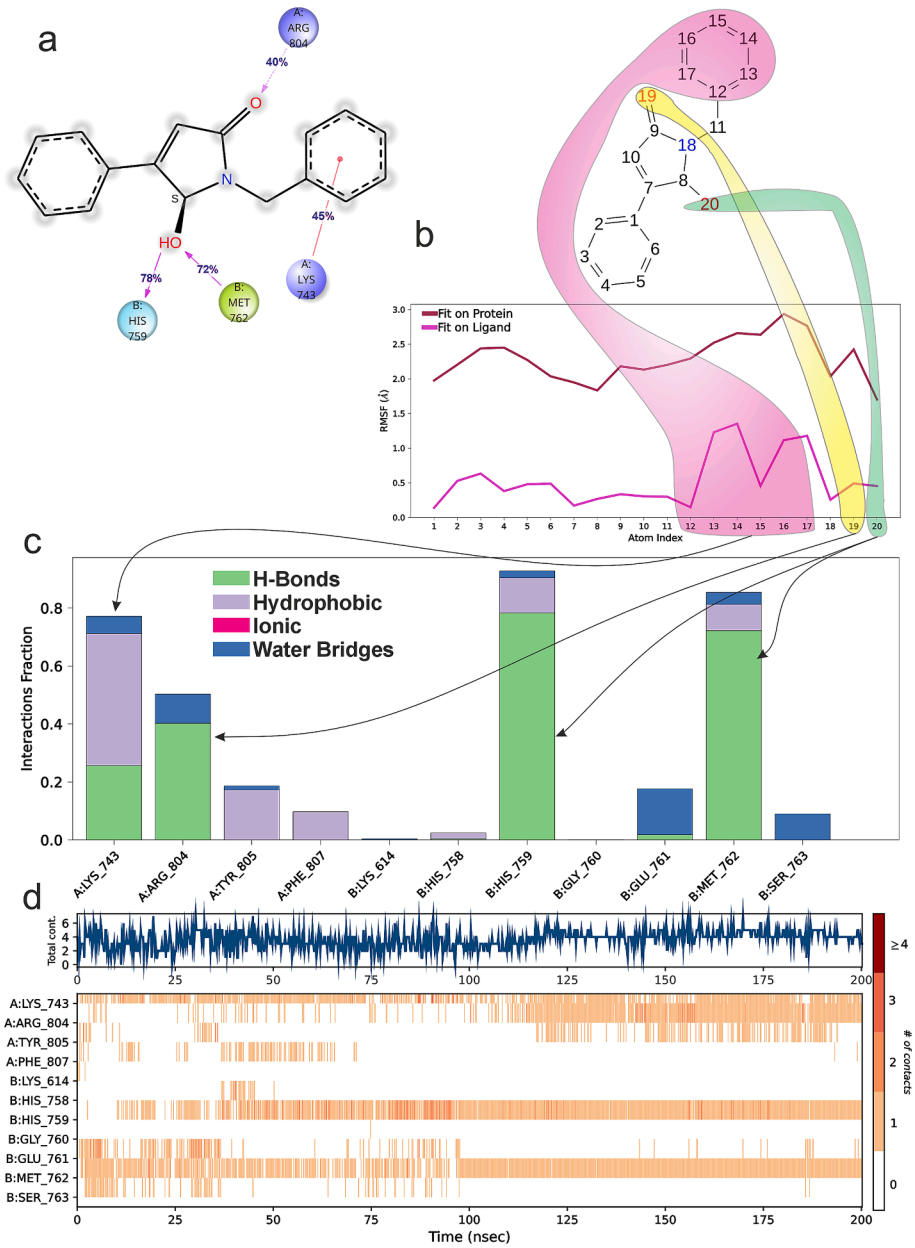

Fig. 10. (**a**) 2D geometrical interactive plot showing interactions of Topoisomerase IIα with compound **2a**. (**b**) L-RMSF depicting the atoms of compound **2a** align with the protein. (**c**) The type of contact strengths is color coded, which represents that the compound **(2a)** binds with Topoisomerase IIα and (**d**) number of contact strength is summarized in a normalized stacked bar chart.

Table 6
Depiction of Physicochemical properties of compounds **2a** and **2b**.

Compounds	MW	#Heavy atoms	#Aromatic heavy atoms	Fraction Csp3	#Rotatable bonds	#H-bond acceptors	#H-bond donors	MR	TPSA
2a	281.43	20	0	1	3	3	2	86.63	43.7
2b	360.33	21	0	1	3	3	2	94.5	43.7

Table 7
Drug likeness, bioactivity, and Synthetic accessibility score of compounds **2a** and **2b.**

Compounds	Lipinski #violations	Ghose #violations	Veber #violations	Egan #violations	Muegge #violations	Bioavailability Score	Brenk #alerts	Synthetic Accessibility
2a	0	0	0	0	0	0.55	0	3.52
2b	0	0	0	0	0	0.55	1	4.3

3.2. Hirshfeld surface (HS) analysis and fingerprint (FP) analysis

Fig. 2 depicts the HS of molecules **2a** and **2b**, with surfaces mapped over normalized contact distance (d_{norm}). The surfaces are shown as translucent to provide a good view of the chemical moiety. The HS analysis revealed distinct intermolecular interactions in both structures. This led us to investigate the role of weak noncovalent forces in crystal packing and the significance of π-π interactions in determining structure organization. In Fig. 2**a**, the bright red spots indicate the existence of OH···H, H···H, and N-H···N intermolecular interactions in compound **2a**. In Fig. 2**b**, the bright red spots indicate the existence of C-H···O and O-H···H intermolecular interactions in compound **2b**.

An examination of HS maps over shape index and curvedness attributes reveals the impact of π-π stacking on molecule assembly. Fig. 3**a** shows red and blue triangles in the same location of the form index surface implying π-π stacking interactions. The blue triangles depict convex areas caused by the presence of the ring carbon atoms within the surface. In contrast, red triangles depict concave areas generated by carbon atoms from rings above the surface. Fig. 3**b** shows a flat area towards the bottom of molecules **2a** and **2b**, indicating π-π stacking which helps contribute to the harmony and stability of the crystalline structure [63,64].

The 2D FP plots for various intermolecular interactions are presented in Fig. 4 and Fig. 5. Table 4 presents an overview of these individual interactions, including reciprocal contacts and their contributions. Table 4 shows that H-H contacts contribute significantly to total HS, accounting for 52.7 % in **2a** and 37.6 % in **2b**. The two big spikes near the bottom of FP suggest strong hydrogen bond interactions between O···H/H···O, which account for 14.2 % and 15.6 % in **2a** and **2b**, respectively. Additionally, the interaction between hydrogen and carbon (C···H/H···C) accounts for 28.8 % and 20.9 % of the total HS in **2a** and **2b**, respectively. The other minor contacts include O···O, C···C, N···H, C···H, C···O, H···Br, C···Br and N···C, which accounts for the remaining percentage of interactions to the total HS.

3.3. Density functional theory (DFT) calculations

3.3.1. Molecular geometry

The optimized molecular geometry of the title molecules were performed using DFT calculations with the B3LYP/6–311++G(d,p) level of theory in solvent (Dichloromethane) phase. Theoretical bond lengths, angles, and torsion angles were matched with XRD results. This work involved both theoretical calculations in the gas phase and experiments in the solid phase. Compared to the experimental data, most theoretical parameters are slightly higher (Table S1, S2 and S3 in supporting information file). The molecular structures of **2a** and **2b**, obtained from XRD and DFT methods have been overlaid and its shown in Fig. 6 with an RMSD value of 0.528 Å for **2a** and 0.045 Å for **2b** (without inversion).

As can be seen from Fig. 6, the molecular structures of **2a** and **2b** overlaid exactly. Also, we can observe that there is a slight deviation in **2a** especially at the hydrogen atom of the OH group. The hydrogen atom of the OH group is twisted away from the plane this is because of the existence of O-H…O intermolecular interactions in the crystal structure.

3.3.2. Frontier molecular orbitals (FMOs) analysis

The HOMO and LUMO are referred to as frontier molecular orbitals. The energy of the HOMO indicates the molecule's ability to donate electrons, while the energy of the LUMO reflects its ability to accept electrons. Analyzing the FMOs and their energy levels is one of the decisive factors in determining molecular electrical properties, including conductivity, chemical reactivity, kinetic stability, biological characteristics, and its potential uses in optoelectronic devices [65].

The compound **2a** structural coordinates **(**Fig. 7**)** are optimized in the solvent effect using the DFT technique with the B3LYP hybrid functional and the 6–311++G(d,p) basis set. **Table S4** displays the calculated frontier molecular orbital energies (E_{HOMO}, E_{LUMO}, and E_g) and chemical reactive descriptors, including ionization potential, electron affinity, electronegativity, global hardness, chemical potential, electrophilicity, chemical softness, and maximum charge transfer (Δn_{max}) [66,67].

The critical elements in evaluating molecular properties are, conductivity, chemical reactivity, kinetic stability, and biological features, and these properties can be predicted based on the study of FMOs of molecules and their energy levels[68]. Molecules with high energy gaps are stable and exhibit moderate chemical reactivity, while those with lower HOMO-LUMO energy gaps are typically more polarizable, conductors, and exhibit high chemical reactivity with low kinetic stability.

The compound **2b** energy level diagram of the FMOs is represented in **(**Fig. 7**)**, and the calculated values of FMOs for **2a** and **2b** are presented in **Table S4**. The calculated energy difference, defined by ΔEgap, is 4.624 eV for molecule **2a** **(**Fig. 7**)**, elucidating the eventual interactions involving charge transfer within the molecules. Other crucial parameters are determined using E_{HOMO} and E_{LUMO} values. On the other hand, for molecule **2b**, ΔEgap measures 4.264 eV **(**Fig. 7**)**. As depicted in **Table S4**, the chemical hardness of **2b** is lower than that of **2a**, indicating higher reactivity for **2b**. Molecule **2b** exhibits pronounced electrophilic characteristics, as evidenced by its higher value than **2a**. ΔN_{max} quantifies the charge an electrophilic system can accept. Thus, the maximum charge transfer is observed for molecule **2b**, attributed to its lower energy gap compared to the other system.

3.3.3. Molecular electrostatic potential (MEP) analysis

MEP maps are three-dimensional diagrams that show the reactive sites and charge distribution of molecules. It demonstrates potential electrophilic and nucleophilic attack sites, making it suitable for biological identification and hydrogen bonding. This calculation helps visualize the polarity of a molecule. The color scale indicates the electrostatic potential region on a molecule's surface, with red being the most electronegative potential, blue representing the most positive potential, and green representing zero potential. Electrostatic potential values increase in the following order: red, green, and blue.

The Fig. 8 depicts that the negative electrostatic potential attracts a proton to the cluster of electron density in the molecule (shades of red), while the positive electrostatic potential repels it to the nuclei (shades of blue). Fig. 8, revealed that the negative regions appear over the oxygen atoms of the carbonyl group and a hydroxyl group, which is the most reactive site for an electrophilic attack, whereas the positive regions appear over the hydrogen atoms of the –OH group and the entire molecule, which are a plausible site for nucleophilic attack. Also, this region validates the intermolecular interactions exhibited in the crystal structure of the two compounds **2a** and **2b**.

3.4. Molecular docking

Molecular docking is a well-established computational technique reliant on structural information that has been extensively applied in drug discovery [69,70]. This method facilitates the discovery of potential therapeutic compounds, foreseeing interactions between ligands and targets on a molecular scale and outlining relationships between structure and activity [71,72]. A series of proteins such as Human Topoisomerase II alpha, PDE3A, JNK2, human 17β-Hydroxysteroid-Dehydrogenase, glutaminase, catalase, JNK1, human KEAP1, human NQO1, GPX4, and ubiquitin were screened for compounds **2a** and **2b**. Among the series of screened proteins, Human Topoisomerase II alpha showed a good docking score against the compound **2a** (−8.33 kcal/mol) and **2b** (−8.47 kcal/mol), followed by PDE3A, and JNK2 (Table 5). Hence, to verify the docking results, compounds **2a** and **2b** complexed with Human Topoisomerase II alpha, PDE3A, and JNK2 were processed for MM/GBSA.

3.5. MM/GBSA

The G_{score} for each ligand **2a** and **2b** was computed against Human

Topoisomerase II alpha, PDE3A, and JNK2 to validate the molecular docking method and predict the behaviour of the ligand–protein complex. The MM/GBSA score is commonly utilized to validate the results of molecular docking. Typically, the biological activity data from a diverse set is correlated with MM/GBSA scoring for an individual ligand against the targeted macromolecule [73]. The results of the MMGBSA were quantified in terms of the $\Delta G_{(binding\ energy)}$, $\Delta G_{(Coulomb)}$, $\Delta G_{(Covalent\ energy)}$, $\Delta G_{(H\text{-}bond)}$, $\Delta G_{(Lipo)}$, and $\Delta G_{(vdW)}$ involved (Table 5). Ligands **2a** and **2b** interacted well with the targeted proteins, such as Human Topoisomerase II alpha, PDE3A, and JNK2, with good G_{score} and hydrogen bond scores. Still, the $\Delta G_{(binding\ energy)}$ in the case of Human Topoisomerase II alpha had a good docking score along with $\Delta G_{(binding\ energy)}$ of −37.54 kcal/mol and −35.42 kcal/mol for ligand **2a** and **2b**, respectively (Table 5). Hence, Human Topoisomerase II alpha complexes with compounds **2a** and **2b** were subjected to MDSs to study the protein and ligand molecular dynamics.

3.6. Molecular dynamics simulations (MDSs)

Each docked complex was studied for molecular dynamics simulation for each selected ligand against the targeted macromolecule [74–76]. When **2a** is bound to Human Topoisomerase II Alpha, the protein and ligand RMSD are stable throughout the MDSs. According to the software, the RMSD of protein and ligand fluctuation are under the permissible level. (Fig. 9**a**). The protein RMSF shows multiple ligand contact points (Fig. 9**b**). The 2D interaction of **2a** with Human Topoisomerase II Alpha depicts that, ligand **2a** forms a hydrogen bond with A-chain of Lys743 and π-π stacking with Arg804. Meanwhile, the B-Chain of Human Topoisomerase II Alpha forms a hydrogen bond with His759 and Met762 (Fig. 10**a**). The L-RMSF for compound **2a** with Human Topoisomerase II Alpha provides a valuable pharmacophore mapping (Fig. 10**b)** with ligand interactions with the polypeptide**.** The type of interactions governed by ligand **2a** is given by the stacked bar graph (Fig. 10**c**), wherein Lys743 imparts hydrogen and hydrophobic interactions (π-π stacking) with the benzylic aromatic ring of ligand **2a**, the alcoholic hydroxyl group of **2a** forms hydrogen bond with His759, and Met762. These are very crucial amino acids during catalysis. The ketone carbonyl group of **2a** forms a hydrogen bond. With the help of a color-coded scale bar, the number and strength of the **2a** contact point with Human Topoisomerase II Alpha are shown, and it can be demonstrated that His756 and Met763 have a close interaction with compound **2a** (Fig. 10**d**). This interaction lasted for 200 ns in the molecular dynamics simulation. Whereas in the case of compound **2b**, the protein and ligand RMSD were stable (Fig. S2**a**), and the Protein RMSF plot showed multiple ligand contact points (Fig. S2**b**). The 2D interaction of compound **2b** with Human Topoisomerase II Alpha shows that Met762 is near the macromolecule (Fig. S3**a**). The L-RMSF plot shows the interactions are not as good as compound **2a** (Fig. S3**b**). During the MDSs with the **2b**- Human Topoisomerase II alpha, it was found that amino acids such as Met762 are present at the proximity of the active site of Human Topoisomerase II alpha (Fig. S3**c**) and Met 762 is only one amino acid which is forming hydrophobic interactions throughout the MDSs (Fig. S3**d**). Different pharmacokinetic descriptors were retrieved *via* Swiss ADME web server to predict physicochemical, pharmacokinetic, ADME, toxicity, and drug-likeness.

3.7. ADME analysis

Physicochemical properties are crucial for the development of novel pharmaceuticals. These properties impact a molecule's pharmacokinetics, pharmacodynamics, bioavailability, and overall drug-likeness profile. These constraints were calculated for compounds **2a** and **2b** as tabulated in Table 6, which provides the compounds **2a** and **2b** physicochemical properties pass through and ability to possess good bioavailibilty. Additionally, the drug-likeness profiles were computed using the following methods: Ghose ($160 \leq MW \leq 480$; $-0.4 \leq WLogP \leq 5.6$; $40 \leq MR \leq 130$ and $20 \leq atoms \leq 70$) provides Ghose filter defines druglikeness constraints which is within the limit for compounds **2a** and **2b**. Compounds **2a** and **2b** follows Lipinski's rule along with the prediction of bioactivity score [32]. These prediction results of **2a** and **2b** were by five rules and standards with a 0.55 bioactivity score depicts the druglikeness (Table 7). Furthermore, the synthetic feasibility of compounds **2a** and **2b** (depicted in **Fig. S4**) was assessed to gauge the complexity of their molecular structures.

4. Conclusion

In the current study, we have explored the conformational characteristics of two gamma lactam derivatives. The ^{1}H NMR and ^{13}C NMR spectral data provided the proton and carbon skeleton of compounds **2a** and **2b** and the mass of the molecular ion peaks in HRMS spectra are exactly matching with the molecular weight of compounds **2a** and **2b**. Single crystal structure analysis of compound **2a** reveals that the crystal packing exhibits intermolecular hydrogen bond interactions, whereas **2b** exhibits both intra and intermolecular hydrogen bond interactions. And also confirms the different substituent on C-4 carbon of pyrrole-2 (5*H*)-one ring in compounds **2a** and **2b** respectively. Due to these structural changes, the analysis of these molecules showed different interactions. The interactions are quantified by Hirshfeld surface analysis, where H···H contacts (52.7 % in **2a** and 37.6 % in **2b**) significantly contribute to the total Hirshfeld surface. The DFT calculation was employed to optimize the structural coordinates and to correlate the results obtained from the experimental findings. The computed structural parameters are well agreed with the experimental results as validated by the structural overlay. Density functional theory (DFT) using implicit solvation models, the energy gap of the FMOs are found to be 4.624 eV in **2a** and 4.264 eV in **2b**, respectively. Further, MEP surface plot revealed the presence of reactive sites in compounds **2a** and **2b**. Molecular docking studies show that compounds **2a** and **2b** are potent against Human Topoisomerase II Alpha, which was further validated using MM/GBSA and MDSs. At the putative binding site of the macromolecule, these compounds **2a** and **2b** form the majority of interactions with the Human Topoisomerase II Alpha by inhibiting the Human Topoisomerase II Alpha activity. In general, the data provided here will be valuable for enhancing the optimization of Human Topoisomerase II Alpha inhibitors in the future. Additionally, compounds **2a** and **2b** may function as drug-like candidates, according to an ADME study.

CRediT authorship contribution statement

Fan Xue: Formal analysis, Data curation. **Habbanakuppe D Preetham:** Methodology. **Rameshwari Verma:** Data curation. **Chandra: . T. N. Lohith: . Sahana Raju:** Formal analysis. **S. Divakara:** Software. **Mohd Sajid Ali:** Investigation. **Hamad A. Al-Lohedan:** Supervision. **Harsha Ramakrishna:** Formal analysis. **Kothanahally S. Sharath Kumar:** Conceptualization. **Vivek Hamse Kameshwar:** Writing – original draft.

Declaration of competing interest

The authors declare that they have no known competing financial interests or personal relationships that could have appeared to influence the work reported in this paper.

Acknowledgments

Science and Technology Natural Science Basic Research Program of Shaanxi Province (No. 2022JQ-134), Ph. D Research Startup Foundation of Yulin University Grant (No. 20GK05); Yulin City Foreign Talent Project (1506-2023KJZG01); Authors acknowledge the financial support through the Researchers Supporting Project number (RSPD2024R724), King Saud University, Riyadh, Saudi Arabia.

Appendix A. Supplementary data

CCDC-2157931 (**2a**) 2157925 (**2b**) contains the supplementary crystallographic data for this article. Supplementary data to this article can be found online at https://doi.org/10.1016/j.cplett.2024.141725.

Data availability

Data will be made available on request.

References

[1] S.B. Singh, M.A. Goetz, E.T. Jones, G.F. Bills, R.A. Giacobbe, L. Herranz, S. Stevens-Miles, D.L. Williams Jr., Oteromycin: A Novel Antagonist of Endothelin Receptor, J. Org. Chem. 60 (1995) 7040–7042.

[2] B. Nay, N. Riache, L. Evanno, Chemistry and biology of non-tetramic γ-hydroxy-γ-lactams and γ-alkylidene-γ-lactams from natural sources, Nat. Prod. Rep. 26 (2009) 1044–1062.

[3] J.E. Baldwin, C. Lowe, C.J. Schofield, E. Lee, A γ-lactam analogue of penems possessing antibacterial activity, Tetrahedron Lett. 27 (1986) 3461–3464.

[4] D.B. Boyd, B.J. Foster, L.D. Hatfield, W.J. Hornback, N.D. Jones, J.E. Munroe, J. K. Swartzendruber, γ-Lactam analogues of carbapenems, Tetrahedron Lett. 27 (1986) 3457–3460.

[5] J.E. Baldwin, R.M. Adlington, R.H. Jones, C.J. Schofield, C. Zaracostas, C. W. Greengrass, γ-Lactam analogues of carbapenicillanic acids, Tetrahedron 42 (1986) 4879–4888.

[6] J. Caruano, G.G. Muccioli, R. Robiette, Biologically active γ-lactams: synthesis and natural sources, Org. Biomol. Chem. 14 (2016) 10134–10156.

[7] E.C. Izgu, T.R. Hoye, Total synthesis of (±)-leuconolam: intramolecular allylic silane addition to a maleimide carbonyl group, Chem. Sci. 4 (2013) 2262–2266.

[8] Y.R. Girish, K.S. Sharath Kumar, K. Prashantha, S. Rangappa, M.S. Sudhanva, Significance of Antioxidants and Methods to Evaluate Their Potency, Mater. Chem. Horiz. 2 (2023) 93–112.

[9] X.-C. Huang, X. Xiao, Y.-K. Zhang, T.T. Talele, A.A. Salim, Z.-S. Chen, R.J. Capon, Lamellarin O, a Pyrrole Alkaloid from an Australian Marine Sponge, Ianthella sp., Reverses BCRP Mediated Drug Resistance in Cancer Cells, Mar. Drugs (2014) 3818–3837.

[10] H. Zhang, M.M. Conte, X.-C. Huang, Z. Khalil, R.J. Capon, A search for BACE inhibitors reveals new biosynthetically related pyrrolidones, furanones and pyrroles from a southern Australian marine sponge, Ianthella sp, Org. Biomol. Chem. 10 (2012) 2656–2663.

[11] S.A. Douglas, M. Gellai, M. Ezekiel, G.Z. Feuerstein, J.D. Elliott, E.H. Ohlstein, Antihypertensive Actions of the Novel Nonpeptide Endothelin Receptor Antagonist SB 209670, Hypertension 25 (1995) 818–822.

[12] Y.-L. Yang, C.-P. Lu, M.-Y. Chen, K.-Y. Chen, Y.-C. Wu, S.-H. Wu, Cytotoxic Polyketides Containing Tetramic Acid Moieties Isolated from the Fungus Myceliophthora Thermophila: Elucidation of the Relationship between Cytotoxicity and Stereoconfiguration, Chem. Eur. J. 13 (2007) 6985–6991.

[13] R.S. Coleman, M.C. Walczak, E.L. Campbell, Total Synthesis of Lucilactaene, A Cell Cycle Inhibitor Active in p53-Inactive Cells, J. Am. Chem. Soc. 127 (2005) 16038–16039.

[14] B.B. Snider, B.J. Neubert, A Novel Biomimetic Route to the 3-Acyl-5-hydroxy-3-pyrrolin-2-one and 3-Acyl-3,4-epoxy-5-hydroxypyrrolidin-2-one Ring Systems, The J. Org. Chem. 69 (2004) 8952–8955.

[15] F. Pin, S. Comesse, B. Garrigues, Š. Marchalín, A. Daïch, Intermolecular and Intramolecular α-Amidoalkylation Reactions Using Bismuth Triflate as the Catalyst, J. Org. Chem. 72 (2007) 1181–1191.

[16] K.S. Sharath Kumar, H. Ananda, S. Rangappa, S.C. Raghavan, K.S. Rangappa, Regioselective competitive synthesis of 3,5-bis(het) aryl pyrrole-2-carboxylates/carbonitriles vs. β-enaminones from β-thioxoketones, Tetrahedron Lett. 82 (2021) 153373.

[17] H. Kakeya, C. Onozawa, M. Sato, K. Arai, H. Osada, Neuritogenic Effect of Epolactaene Derivatives on Human Neuroblastoma Cells Which Lack High-Affinity Nerve Growth Factor Receptors, J. Med. Chem. 40 (1997) 391–394.

[18] J. Clayden, R. Turnbull, I. Pinto, Diastereoselective protonation of extended pyrrol-3-en-2-one enolates: an attempted 'de-epimerisation', Tetrahedron: Asymmetry 16 (2005) 2235–2241.

[19] H.D. Preetham, U. Muddegowda, K.S. Sharath Kumar, S. Rangappa, K.S. Rangappa, Identification of β-aminopyrrolidine containing peptides as β-amyloid aggregation inhibitors for Alzheimer's disease, J. Pept. Sci. 28 (2022) e3386.

[20] M. Adib, M. Mahdavi, M.A. Noghani, H.R. Bijanzadeh, Reaction between isocyanides and chalcones: an efficient solvent-free synthesis of 5-hydroxy-3,5-diaryl-1,5-dihydro-2H-pyrrol-2-ones, Tetrahedron Lett. 48 (2007) 8056–8059.

[21] N. Mase, T. Nishi, M. Hiyoshi, K. Ichihara, J. Bessho, H. Yoda, K. Takabe, Regioselective reduction of maleimide and citraconimide derivatives: general preparation of 5-hydroxy-1,5-dihydropyrrol-2-one, J. Chem. Soc. Perkin Trans. 1 (2002) 707–709.

[22] H.D. Preetham, K.S. Sharath Kumar, A. Kandaswamy, S. Rangappa, M.K. Gatasheh, U. Muddegowda, K.S. Rangappa, Alternative Approach to Access 5-Hydroxy-1H-pyrrol-2-(5H)-ones from Base-Induced Tandem Intramolecular Cyclization of Sulfur Ylide with Ketones and 1,3-Hydroxy Rearrangement. ACS, Omega 8 (2023) 48251–48257.

[23] M.E. Wall, M.C. Wani, C.E. Cook, K.H. Palmer, A.T. McPhail, G.A. Sim, Plant Antitumor Agents. I. The Isolation and Structure of Camptothecin, a Novel Alkaloidal Leukemia and Tumor Inhibitor from Camptotheca acuminata1,2, J. Am. Chem. Soc. 88 (1966) 3888–3890.

[24] G. Kohlhagen, K.D. Paull, M. Cushman, P. Nagafuji, Y. Pommier, Protein-linked DNA strand breaks induced by NSC 314622, a novel noncamptothecin topoisomerase I poison, Mol. Pharmacol. 54 (1998) 50–58.

[25] E. Kiselev, D. Sooryakumar, K. Agama, M. Cushman, Y. Pommier, Optimization of the lactam side chain of 7-azaindenoisoquinoline topoisomerase I inhibitors and mechanism of action studies in cancer cells, J. Med. Chem. 57 (2014) 1289–1298.

[26] A. Morrell, M.S. Placzek, J.D. Steffen, S. Antony, K. Agama, Y. Pommier, M. Cushman, Investigation of the Lactam Side Chain Length Necessary for Optimal Indenoisoquinoline Topoisomerase I Inhibition and Cytotoxicity in Human Cancer Cell Cultures, J. Med. Chem. 50 (2007) 2040–2048.

[27] M. Brindisi, L. Frattaruolo, R. Mancuso, A. Palumbo Piccionello, I. Ziccarelli, M. Catto, O. Nicolotti, C.D. Altomare, B. Gabriele, A.R. Cappello, Anticancer potential of novel α, β-unsaturated γ-lactam derivatives targeting the PI3K/AKT signaling pathway, Biochem. Pharmacol. 190 (2021) 114659.

[28] H.K. Swedan, A.E. Kassab, E.M. Gedawy, S.E. Elmeligie, Topoisomerase II inhibitors design: Early studies and new perspectives, Bioorg. Chem. 136 (2023) 106548.

[29] A. Hanke, R. Ziraldo, S.D. Levene, DNA-Topology Simplification by Topoisomerases, Molecules 26 (2021) 3375.

[30] J.L. Delgado, C.-M. Hsieh, N.-L. Chan, H. Hiasa, Topoisomerases as Anticancer Targets. Biochemical J. 475 (2018) 373–398.

[31] K.R. Hande, Topoisomerase II inhibitors, Update on Cancer Ther. 3 (2008) 13–26.

[32] R.D. Jawarkar, A.N. Khan, D.R. Bhagat, P.N. Khatale, P.V. Burakale, S. Farooqui, S. N. Mali, Molecular docking, QSAR, and ADME studies of some pyrrolo[1, 2-a] benzimidazole-based quinones as novel topoisomerase 2 beta (TOP2β) inhibitors, Chem. Phys. Impact 8 (2024) 100479.

[33] Y. Hu, Z. Liu, G. Zha, S. Long, M.B. Sridhara, K.S.S. Kumar, K.P. Rakesh, Triazole derivatives as potential antifungal agents: A structure-activity relationship (SAR) studies, Process Biochem. 135 (2023) 102–118.

[34] J. Wang, S. Long, Z. Liu, K.P. Rakesh, R. Verma, S.K. Verma, K.S. Sharath Kumar, Structure-activity relationship studies of thiazole agents with potential anti methicillin-resistance Staphylococcus aureus (MRSA) activity, Process Biochem. 132 (2023) 13–29.

[35] X. Zhao, R. Verma, M.B. Sridhara, K.S. Sharath Kumar, Fluorinated azoles as effective weapons in fight against methicillin-resistance staphylococcus aureus (MRSA) and its SAR studies, Bioorg. Chem. 143 (2024) 106975.

[36] Y. Sert, M.R. Albayati, F. Şen, N. Dege, The DFT and in-silico analysis of 2, 2′-((1e, 1′ e)-((3, 3′-dimethyl-[1, 1′-biphenyl]− 4, 4′ diyl) bis (azanylylidene)) bis (methanylylidene)) diphenol molecule, Colloids Surf. a: Physicochem. Eng. Asp. 687 (2024) 133444.

[37] N. Dege, H. Gökce, O.E. Doğan, G. Alpaslan, T. Ağar, S. Muthu, Y. Sert, Quantum computational, spectroscopic investigations on N-(2-((2-chloro-4, 5-dicyano-phenyl) amino) ethyl)-4-methyl benzenesulfonamide by DFT/TD-DFT with different solvents, molecular docking and drug-likeness researches, Colloids Surf. a: Physicochem. Eng. Asp. 638 (2022) 128311.

[38] Y. Ait Elmachkouri, Y. Sert, E. Irrou, E.H. Anouar, H. Ouachtak, J.T. Mague, N.K. Sebbar, E.M. Essassi, M. Labd Taha. Synthesis, X-Ray Diffraction, Spectroscopic Characterization, Hirshfeld Surface Analysis, Molecular Docking Studies, and DFT Calculation of New Pyrazolone Derivatives. Polycycl. Aromat. Comp. 44, (2024), 2598-2619.

[39] G.M. Sheldrick, A short history of SHELX, Acta Crystallogr. A 64 (2008) 112–122.

[40] G. Sheldrick, Crystal structure refinement with SHELXL, Acta Crystallogr. C 71 (2015) 3–8.

[41] A.L. Spek, Structure validation in chemical crystallography. Acta crystallogr. D, Biol. crystallogr. 65 (2009) 148-55.

[42] C.F. Macrae, I. Sovago, S.J. Cottrell, P.T.A. Galek, P. McCabe, E. Pidcock, M. Platings, G.P. Shields, J.S. Stevens, M. Towler, P.A. Wood, Mercury 4.0: from visualization to analysis, design and prediction, J. Appl. Crystallogr. 53 (2020) 226–235.

[43] M.A. Spackman, D. Jayatilaka, Hirshfeld surface analysis, CrystEngComm 11 (2009) 19–32.

[44] M.A. Spackman, J.J. McKinnon, Fingerprinting intermolecular interactions in molecular crystals, CrystEngComm 4 (2002) 378–392.

[45] P.R. Spackman, M.J. Turner, J.J. McKinnon, S.K. Wolff, D.J. Grimwood, D. Jayatilaka, M.A. Spackman, CrystalExplorer: a program for Hirshfeld surface analysis, visualization and quantitative analysis of molecular crystals, J. Appl. Crystallogr. 54 (2021) 1006–1011.

[46] M.J. Frisch, G.W. Trucks, H.B. Schlegel, G.E. Scuseria, M.A. Robb, J.R. Cheeseman, G. Scalmani, V. Barone, B. Mennucci, G.A. Petersson, H. Nakatsuji, M. Caricato, X. Li, H.P. Hratchian, A.F. Izmaylov, J. Bloino, G. Zheng, J.L. Sonnenberg, M. Hada, M. Ehara, K. Toyota, R. Fukuda, J. Hasegawa, M. Ishida, T. Nakajima, Y. Honda, O. Kitao, H. Nakai, T. Vreven, J.A. Montgomery Jr., J.E. Peralta, F. Ogliaro, M. Bearpark, J.J. Heyd, E. Brothers, K.N. Kudin, V.N. Staroverov, R. Kobayashi, J. Normand, K. Raghavachari, A. Rendell, J.C. Burant, S.S. Iyengar, J. Tomasi, M. Cossi, N. Rega, J.M. Millam, M. Klene, J.E. Knox, J.B. Cross, V. Bakken, C. Adamo, J. Jaramillo, R. Gomperts, R.E. Stratmann, O. Yazyev, A.J. Austin, R. Cammi, C. Pomelli, J.W. Ochterski, R.L. Martin, K. Morokuma, V.G. Zakrzewski, G.A. Voth, P. Salvador, J.J. Dannenberg, S. Dapprich, A.D. Daniels, O. Farkas, J. B. Foresman, J.V. Ortiz, J. Cioslowski, D.J. Fox, Gaussian 09, Revision B.01, Gaussian Inc., Wallingford, 2010.

[47] R. Dennington, T. Keith, J. Millam, Gauss View, Version 5, Semichem Inc., Shawnee Mission, 2009.

[48] M. Cossi, V. Barone, R. Cammi, J. Tomasi, Ab initio study of solvated molecules: a new implementation of the polarizable continuum model, Chem. Phys. Lett. 255 (4–6) (1996) 327–335.

[49] J. Tirado-Rives, W.L. Jorgensen, Performance of B3LYP density functional methods for a large set of organic molecules, J. Chem. Theory Comput. 4 (2) (2008) 297–306.

[50] F. De Proft, S. Liu, R.G. Parr, Chemical potential, hardness, hardness and softness kernel and local hardness in the isomorphic ensemble of density functional theory, J. Chem. Phys. 107 (8) (1997) 3000–3006.

[51] K. Ravi Singh, T.N. Lohith, T. Ananth Nag, M.A. Sridhar, M.P. Sadashiva, Structure property relationship in two thiazole derivatives: Insights of crystal structure, Hirshfeld surface, DFT, QTAIM, NBO and molecular docking studies, Mol. Cryst. Liq. Cryst. 763 (1) (2023) 54–72.

[52] Y. Jiang, K.P. Rakesh, N.S. Alharbi, H.K. Vivek, H.M. Manukumar, Y.H. E. Mohammed, H.-L. Qin, Radical scavenging and anti-inflammatory activities of (hetero)arylethenesulfonyl fluorides: Synthesis and structure-activity relationship (SAR) and QSAR studies, Bioorg. Chem. 89 (2019) 103015.

[53] D. Shivakumar, J. Williams, Y. Wu, W. Damm, J. Shelley, W. Sherman, Prediction of Absolute Solvation Free Energies using Molecular Dynamics Free Energy Perturbation and the OPLS Force Field, J. Chem. Theory Comput. 6 (2010) 1509–1519.

[54] M. Jyothi, H.A. Khamees, S.M. Patil, R. Ramu, S.A. Khanum, Microwave-Assisted Synthesis, Characterization, Docking Studies and Molecular Dynamic of Some Novel Phenyl Thiazole Analogs as Xanthine Oxidase Inhibitor, J. Iran. Chem. Soc. 19 (2022) 3919–3933.

[55] M.G. Prabhudeva, H.K. Vivek, K.A. Kumar, Synthesis of novel pyrazole carboxamides using reusable catalyst as antimicrobial agents and molecular docking studies, Chem. Data Coll. 20 (2019) 100193.

[56] C. Mallick, M. Mishra, V. Asati, V. Kashaw, R. Das, K.S. Kashaw, *In silico*-Based Structural Prediction, Molecular Docking and ADMET Analysis of Novel Imidazo-Quinoline Derivatives as Pf Purine Nucleoside Phosphorylase Inhibitors, Curr. Signal Transduct. Ther. 18 (2023) 24–53.

[57] P.A. Greenidge, C. Kramer, J.-C. Mozziconacci, R.M. Wolf, MM/GBSA Binding Energy Prediction on the PDBbind Data Set: Successes, Failures, and Directions for Further Improvement, J. Chem. Inf. Model. 53 (2013) 201–209.

[58] J. Li, R. Abel, K. Zhu, Y. Cao, S. Zhao, R.A. Friesner, The VSGB 2.0 model: A next generation energy model for high resolution protein structure modeling, Proteins: Struct. Funct. Bioinf. 79 (2011) 2794–2812.

[59] Y. Wu, L. Lou, Z.-R. Xie, A Pilot Study of All-Computational Drug Design Protocol-From Structure Prediction to Interaction Analysis, Front. Chem. 8 (2020).

[60] Y.R. Girish, B.M.A. Kumar, K.S.S. Kumar, V.K. Hamse, K. Prashantha, M. S. Sudhanva, R. Shobith, Identification of novel benzimidazole-based small molecule targeting dual targets Tankyrase and Bcl2 to induce apoptosis in Colon cancer, J. Mol. Struct. 1269 (2022) 133813.

[61] K.S. Suryakoppa, K. Vivek Hamse, R. Appadurai, S. Eranna, M.H.M. Khan, Enantiomeric Separation of Indole-3-Propanamide Derivatives by Using Supercritical Fluid Chromatography on a Polysaccharide-Based Chiral Stationary Phase, J. Chromatogr. Sci. 60 (2022) 692–704.

[62] A. Daina, O. Michielin, V. Zoete, SwissADME: a free web tool to evaluate pharmacokinetics, drug-likeness and medicinal chemistry friendliness of small molecules, Sci. Rep. 7 (2017) 42717.

[63] M.H. Mrad, C. Ayari, A.A. Alotaibi, H.E. Gomaa, S. Tale Almutairi, S. Gatfaoui, U. Böhme, F. Lefebvre, C. Ben Nasr, Synthesis, structure, surface analysis, molecular docking, physico-chemical characteristics, and DFT calculus discussion of a novel hybrid perovskite material: $(C_5H_6ClN_2)_2HgCl_4$, Inorg. Chem. Comm. 160 (2024) 111966.

[64] N. Shikhaliyev, S. Çelikesir, M. Akkurt, K. Bagirova, G. Suleymanova Atakishiyeva, F. Toze, Crystal structure and Hirshfeld surface analysis of (E)-1-(4-chlorophenyl)-2-[2,2-dichloro-1-(4-fluorophenyl)ethenyl]diazene, Acta Crystallogr. E Crystallogr. Commun. 75 (2019) 465–469.

[65] T.N. Lohith, S. Shamanth, M.A. Sridhar, K. Mantelingu, N.K. Lokanath, Synthesis, molecular structure, Hirshfeld surface, energy framework and DFT studies of 1,3,4 oxadiazole derivative, J. Mol. Struct. 1252 (2022) 132203.

[66] C.G. Zhan, J.A. Nichols, D.A. Dixon, Ionization potential, electron affinity, electronegativity, hardness, and electron excitation energy: molecular properties from density functional theory orbital energies. J. Phys. Chem. A, 107(20), (2003).4184-4195.

[67] J. Chakkamalayath, K.R.S. Chandrakumar, S.K. Ghosh, Reactivity parameters and substitution effect in organic acids, J. Phys. Chem. A 124 (19) (2020) 3770–3777.

[68] K.M. Chandini, F.H. Al-Ostoot, T.N. Lohith, M.Q.A. Al-Gunaid, B.M. Al-Maswari, M.A. Sridhar, S.A. Khanum, Synthesis, structure elucidation, Hirshfeld surface analysis, energy frameworks and DFT studies of novel ethyl 2-(5-methyl-2-oxopyridin-N-yl)acetate (OPA), J. Mol. Struct. 1270 (2022) 133928.

[69] H.D. Preetham, M. Umashankara, K.S.S. Kumar, S. Rangappa, K.S. Rangappa, Pyrrolidine-based cationic γ-peptide: a DNA-binding molecule works as a potent anti-gene agent, Med. Chem. Res. 31 (2022) 507–516.

[70] B. Nagendra Chowdary, H.D. Preetham, S.K. Verma, V.K. Hamse, M. Umashankara, S. Niranjan Raj, K. Pramoda, K.S.S. Kumar, G. Selvi, A short hydrophobic peptide conjugated 3,5- disubstituted pyrazoles as antibacterial agents with DNA gyrase inhibition, J. Mol. Struct. 1276 (2023) 134661.

[71] L. Pinzi, G. Rastelli, Molecular Docking: Shifting Paradigms in Drug Discovery, Int. J. Mol. Sci. 20 (2019) 4331.

[72] S.K. Verma, S. Rangappa, R. Verma, F. Xue, S. Verma, K.S. Sharath Kumar, K. S. Rangappa, Sulfur (S^{VI})-containing heterocyclic hybrids as antibacterial agents against methicillin-resistant Staphylococcus aureus (MRSA) and its SAR, Bioorg. Chem. 145 (2024) 107241.

[73] P.D. Lyne, M.L. Lamb, J.C. Saeh, Accurate Prediction of the Relative Potencies of Members of a Series of Kinase Inhibitors Using Molecular Docking and MM-GBSA Scoring, J. Med. Chem. 49 (2006) 4805–4808.

[74] K.Y. Wong, J. Gao, The reaction mechanism of paraoxon hydrolysis by phosphotriesterase from combined QM/MM simulations, Biochemistry 46 (2007) 13352–13369.

[75] T.S. Lee, C. Silva López, G.M. Giambasu, M. Martick, W.G. Scott, D.M. York, Role of Mg^{2+} in hammerhead ribozyme catalysis from molecular simulation, J. Am. Chem. Soc. 130 (2008) 3053–3064.

[76] N.C. Suresh, B.M.A. Kumar, H.D. Preetham, S.M. Srinivasa, M.S. Ali, H.A. Al-Lohedan, K.S.S. Kumar, C. Shivamallu, A. Jain, S. Rangappa, M. Umashankara, K. Mantelingu, Synthesis, molecular docking and pharmacological studies of novel quinoline derivative as anticancer agent that targets topoisomerase IIB, J. Mol. Struct. 1312 (2024) 138519.